Bull Earthquake Eng (2008) 6:213–239
DOI 10.1007/s10518-007-9055-0

ORIGINAL RESEARCH PAPER

Behaviour of deep immersed tunnel under combined normal fault rupture deformation and subsequent seismic shaking

Ioannis Anastasopoulos · Nikos Gerolymos · Vasileios Drosos · Takis Georgarakos · Rallis Kourkoulis · George Gazetas

Received: 22 June 2007 / Accepted: 25 November 2007 / Published online: 18 December 2007

Abstract Immersed tunnels are particularly sensitive to tensile and compressive deformations such as those imposed by a normal seismogenic fault rupturing underneath, and those generated by the dynamic response due to seismic waves. The paper investigates the response of a future 70 m deep immersed tunnel to the consecutive action of a major normal fault rupturing in an earthquake occurring in the basement rock underneath the tunnel, and a subsequent strong excitation from a different large-magnitude seismic event that may occur years later. Non-linear finite elements model the quasi-static fault rupture propagation through the thick soil deposit overlying the bedrock and the ensuing interaction of the rupture with the immersed tunnel. It is shown that despite imposed bedrock offset of 2 m, net tension or excessive compression between tunnel segments could be avoided with a suitable design of the joint gaskets. Then, the already deformed ("injured") structure is subjected to strong asynchronous seismic shaking. The thick-walled tunnel is modelled as a 3-D massive flexural beam connected to the soil through properly-calibrated nonlinear interaction springs and dashpots, the supports of which are subjected to the free-field acceleration time histories. The latter, obtained with 1-D wave propagation analysis, are then modified to account for *wave passage* effects. The joints between tunnel segments are modeled with special non-linear hyper-elastic elements, properly accounting for their 7-bar longitudinal hydrostatic pre-stressing. Sliding is captured with special gap elements. The effect of segment length and joint properties is explored parametrically. A fascinating conclusion emerges in all analysed cases for the joints between segments that were differentially deformed after the quasi-static fault rupture: upon subsequent very strong seismic shaking, overstressed joints de-compress and understressed joints re-compress—a "healing" process that leads to a more uniform deformation profile along the tunnel. This is particularly beneficial for the precariously de-compressed joint gaskets. Hence, the safety of the immersed tunnel improves with "subsequent" strong seismic shaking!

I. Anastasopoulos · N. Gerolymos · V. Drosos · T. Georgarakos · R. Kourkoulis · G. Gazetas (✉)
School of Civil Engineering, National Technical University of Athens, Heroon Polytechniou 9, 15780 Zografou, Athens, Greece
e-mail: gazetas@ath.forthnet.gr

Keywords Immersed tunnel · Fault rupture propagation · Dynamic analysis · Earthquake · Soil–structure interaction · Fault rupture–soil–tunnel interaction

1 Introduction

The objective of this paper is to investigate the behaviour of a deep immersed tunnel under the combined action of a major fault rupturing underneath, and subsequent strong seismic shaking. The presented research is part of a feasibility study for a railway immersed tunnel in the Rion–Antirrion straits, in Greece. The construction of the tunnel will be a technological challenge, due to the combination of great water depth (67 m; presently the world record), very high seismicity, and deep alluvial soils. At the narrowest crossing of the Corinthian Gulf trench, which is characterised by an extensional slip rate of about 1 cm/year, the tunnel will unavoidably cross at least one active fault. It must be capable of safely undertaking the ensuing permanent ground deformation.

Moreover, in the 100-year design life of the tunnel, strong seismic shaking from another earthquake, originating at a different major fault located not directly under the site, is a distinct possibility given the numerous active faults in the Corinthian and Patraicos Gulfs, as well as in their neighboring regions. Such seismic shaking will find the immersed tunnel already "injured" from the faulting-induced deformation of the first seismic event (which will have occurred perhaps several 10s of years earlier). It is crucial for a successful design to ensure that the permanent tensile deformation due to the normal-fault rupture, and the superimposed subsequent dynamic deformation during shaking will not jeopardize the water-tightness of the tunnel at any moment. Figure 1 sketches the two loading situations studied in the paper.

2 A future Rion–Antirrion railway link

The feasibility of a railway link of the Rion–Antirrion straits in Greece is being explored (Fig. 2). The straits will be crossed at approximately 300 m east of the recently built cable-stayed road bridge. At this narrowest point, the under-water length is about 2.5 km, with a maximum depth of 70 m, nearly constant for about 1 km (Fig. 3). A hybrid tunneling solution has been developed combining a 1-km central immersed tunnel at the deepest section of the crossing, with two bored "approach" tunnels (of about 8 km total length) at the two sides.

Designed to accommodate two-way rail traffic, the immersed tube will be about 24 m wide and 11 m high. While more design details can be found in Anastasopoulos et al. (2007a), it is emphasised here that the huge hydrostatic loading necessitates that walls be 1.5 m thick. The longitudinal cross section of the central immersed part is depicted in Fig. 3, along with an indicative soil classification and N_{SPT} blow counts, based on the exploration that had been conducted for the neighboring bridge. The soil consists of alternating layers of sandy gravel to gravel, silty sand and clay, of medium density and stiffness. The geotechnical exploration reached a maximum depth of 100 m below the seabed, without encountering bedrock. A detailed geophysical tomography (Tselentis et al. 2004) revealed that limestone bedrock ($V_p > 3,500$ m/s) lies at about 800 m depth. Geophysical data and earlier shear wave velocity V_s measurements were utilised to derive six idealised soil profiles.

The Rion–Antirron straits, the narrowest crossing of the Corinthian Gulf trench, is associated with a tensile tectonic environment of N–S direction, expressed by a sequence of normal faults of E–W strike, dipping towards the axis of the trench (Fig. 2). Being a very active seismic zone, it has been the source of five $M_s > 6$ earthquakes in the last 30 years. The most

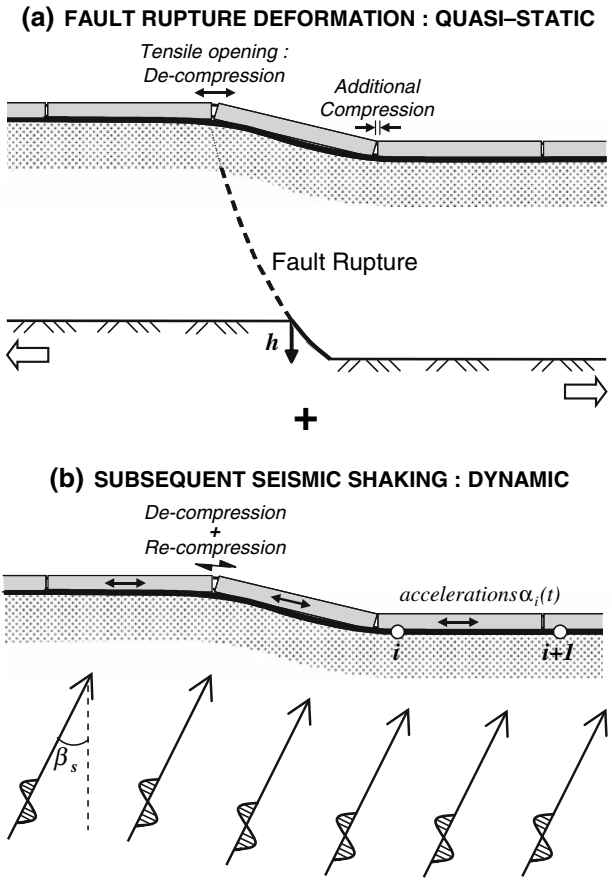

Fig. 1 Problem definition—the two critical types of seismic loading that may take place in the life of the tunnel: (**a**) quasi-static deformation due to normal fault rupture underneath the tunnel and (**b**) subsequent strong seismic shaking in the form of shear wave incident at an angle β_S

recent event was the M_s 6.4 Aegion 1995 earthquake (Bernard et al. 1997; Gazetas 1996), with an epicentral distance of 28 km from the site. The straits are also affected by more distant seismogenic zones.

3 Seismic design of the proposed immersed tunnel

Until today, no immersed tunnel is known to have ever been "hit" by an underneath rupturing fault. On the other hand, two immersed tunnels have been subjected to fairly strong seismic shaking: the Bay Area Rapid Transit (BART) tunnel in California, and the Osaka South Port (OSP) immersed tunnel in Japan. Both tunnels behaved exceptionally well, sustaining no measurable damage. BART, built in the 60s, was one of the first underground structures designed against seismic loading and equipped with special 3-dimensional joints (Kuesel 1969; Douglas and Warshaw 1971; Bickel and Tanner 1982). It survived the 1989 Loma Prieta M_s 7.1 earthquake with no damage, sustaining only a small relative displacement between

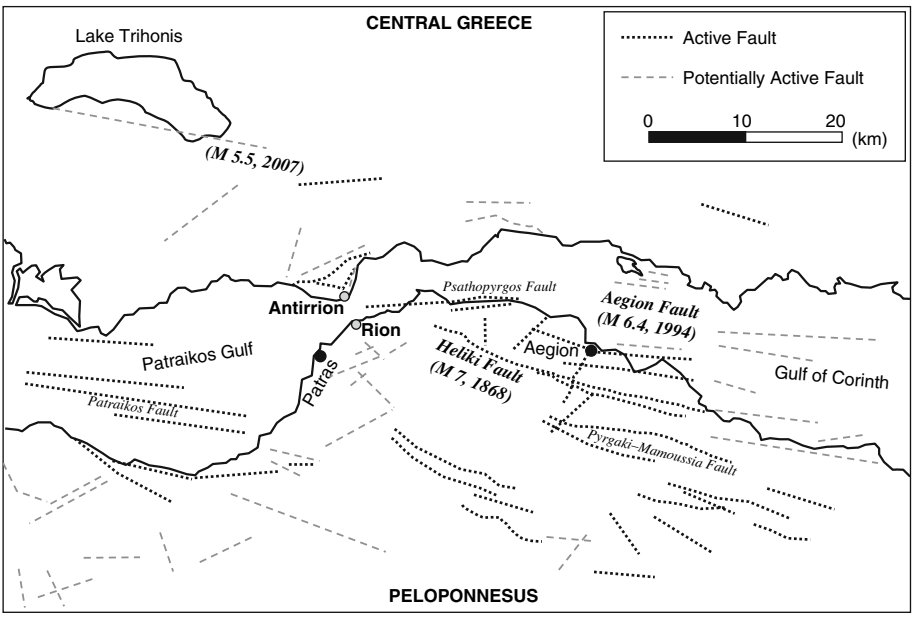

Fig. 2 Rion–Antirrion straits, along with active and potentially active faults, and the magnitudes of some recent earthquakes

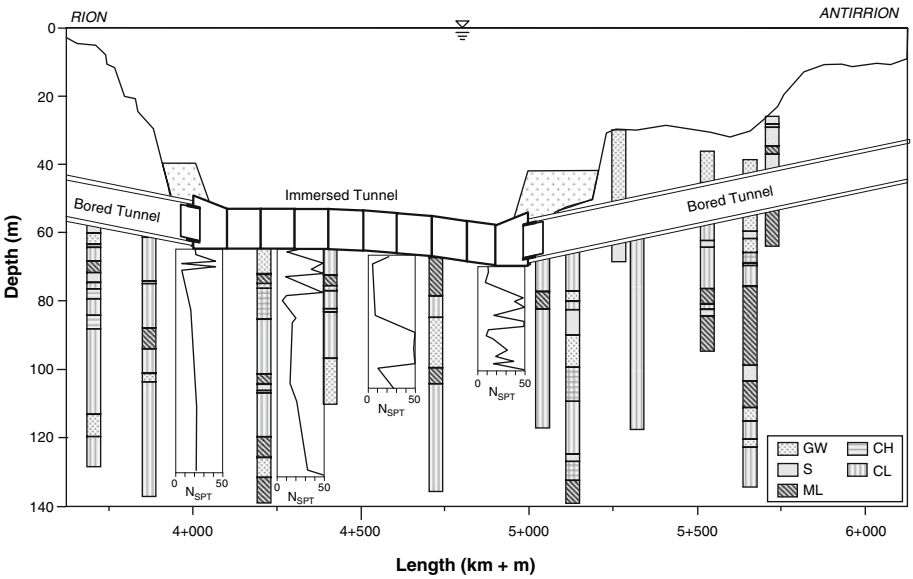

Fig. 3 Longitudinal section of the proposed tunnel, along with indicative soil classification and N_{SPT} blow counts, based on available geotechnical data

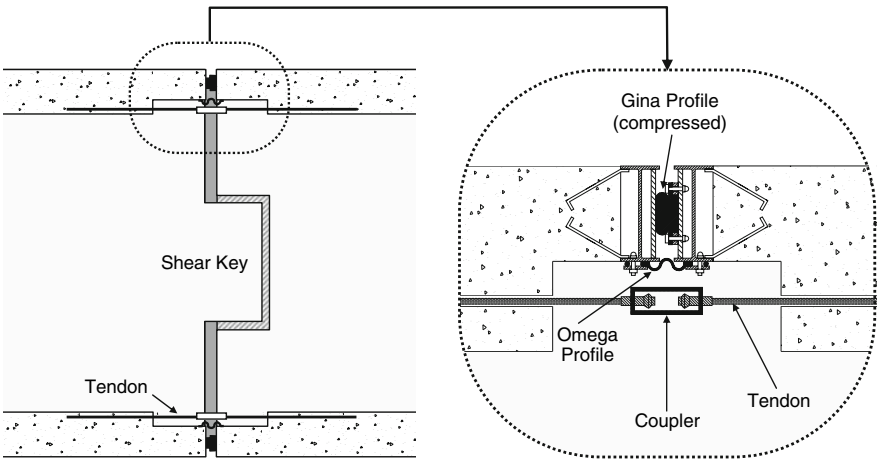

Fig. 4 Schematic illustration of the aseismic design of immersion joints: gina gasket are compressed during installation, providing the necessary water-tightness; omega seals and tendons with couplers are used as secondary protection measures; shear-keys are installed to restrict lateral and vertical differential displacements between consecutive segments

end segments and approach structures (PB 1991). OSP performed also exceptionally during the 1995 M_{JMA} 7.2 Kobe earthquake. While the above tunnels are located at shallow depths, we note the recent trend of installing immersed tunnels at great depths, such as the currently under construction Bosporus Crossing immersed tunnel in Istanbul (56 m deep, 1.5 km long) and the South Korean Car Tunnel (47 m deep, 3 km long).

The proposed design of the studied tunnel is similar to that of the Osaka South Port tunnel (Fig. 4). The precast concrete segments, floated over a pre-excavated trench, will be lowered with the help of special sinking rigs. Once the two segments gain contact, the water between them will be drained, and the Gina gasket will be compressed due to one-sided hydrostatic water pressure, achieving the necessary water-tightness. Given the 650 kPa (6.5 bar) pressure, the use of the largest available Gina gasket is unavoidable: under compressive loading, rubber gaskets may fail due to tensile lateral strains (a Poisson type effect; see Kelly 1997). Although the largest available Gina section is estimated to be capable of undertaking the loading, special analysis and testing will be a prerequisite for acceptance. Secondary lines of defense include the "*omega*" *seal* and longitudinal *tendons*. But since none of them can sustain substantial shear, "*shear keys*" are also constructed once the segments have been connected.

The scope of this paper is to analyse the behaviour of the tunnel under a sequence of: (a) normal fault-induced displacement, and (b) subsequent strong seismic shaking. The behaviour of the tunnel subjected to a variety of seismic shaking scenarios has been investigated in Anastasopoulos et al. (2007a). It was shown that the tunnel could safely resist a variety of soil-amplified strong excitations, of PGA as large as 0.60 g, PGV as large as 80 cm/s, and containing long–period pulses. In the present paper we parametrically investigate three possible segment lengths: 70, 100, and 165 m. While the modern economic trend (e.g. Marshall 1999) is to use longer segments, the combination of such depth (67 m) with the vivid tectonic environment make the technical feasibility the foremost priority of the design.

The type of Gina gasket is also parametrically investigated, as the longitudinal deformation of the tunnel depends on its properties, and ensuring its impermeability is critical.

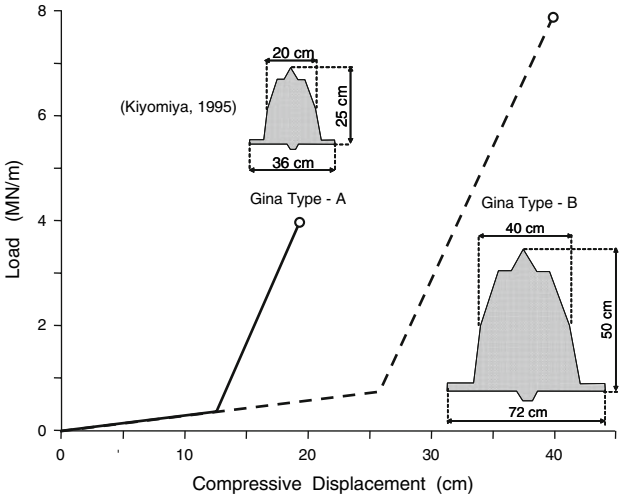

Fig. 5 Hyperelastic force–displacement backbone curves of rubber joints used in the analysis: Type A refers to the largest available GINA gasket, estimated based on half-scale tests of Kiyomiya (1995); Type B is a hypothetical logical projection

Fault-induced extension and differential settlement will unavoidably decompress at least some of the joints. Additionally, during a subsequent strong seismic event, that may occur years later, the longitudinal vibration of the tunnel will subject the immersion joints to cyclic (dynamic) re-compression and de-compression. The magnitude of the total de-compression is critical for the design of the tendons. If such de-compression is significant, the tendons will have to engage, undertaking large tensile forces to ensure water-tightness. The problem is that such tensile loads will eventually be undertaken by the concrete, leading to unavoidable cracking and loss of water-tightness.

Two types of joints (Fig. 5) are parametrically investigated. Type A refers to the idealised behaviour of the largest currently available Gina profile, while type B is a hypothetical double-sized Gina-type gasket. The behaviour of this hypothetical gasket provides wider deformation limits, permitting significant additional compression and de-compression. The hyper-elastic load-displacement backbone curves of the two types of gasket are estimated on the basis of test results of half-sized models (Kiyomiya 1995).

Another problem parameter is the shear-key "*allowance*": if large enough, some differential transverse displacement between consecutive segments will be allowed; its reduction will lead to a more-or-less "fixed" connection. Although its effect has already been shown to be minor (Anastasopoulos et al. 2007a), it is parametrically investigated for completeness. Two extreme values are explored: 5 and 20 mm.

4 Methodology of analysis

The finite element code ABAQUS (2004) is utilised to perform non-linear quasi-static and dynamic transient analysis of the tunnel. The layout of the model is depicted in Fig. 6. The immersed tunnel is modeled as a series of beams connected to the soil through interaction springs and dashpots. Tunnel segments are modeled with special beam elements that take account of shear rigidity. As discussed in detail in Anastasopoulos et al. (2007a), each

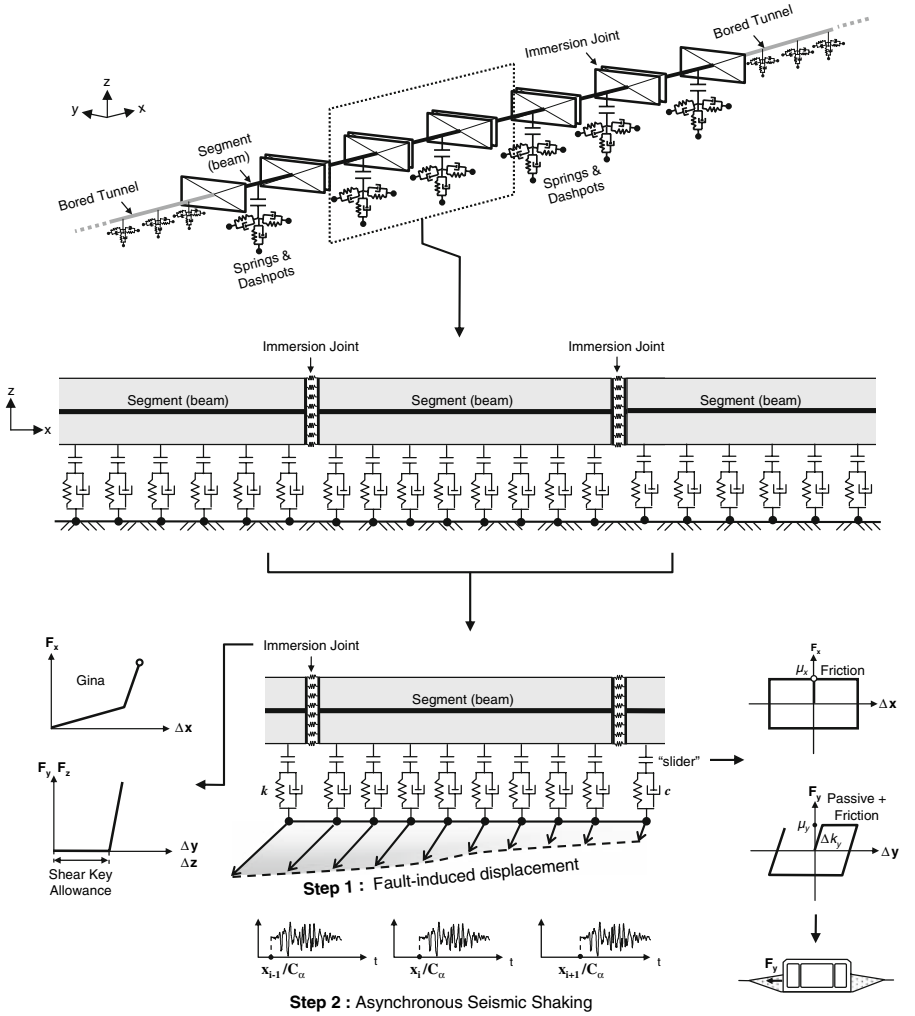

Fig. 6 Finite element modeling layout: in the first step, the fault-induced displacements are applied to the tunnel quasi-statically. Then, in a second step we apply the asynchronous seismic excitation

immersion joint is modeled with special 64-node frames representing the perimeter of the tube–collar connection. Adjacent frames are connected with each other with non-linear hyper-elastic springs, simulating the behaviour of the segment joints.

The analysis is conducted in three steps:

- In "*Step 0*" the hydrostatic pressure is applied statically to the end of each segment, to simulate the initial hydrostatic compression. The details of the installation procedure, along with a discussion on time-dependent stress relaxation effects can be found in Anastasopoulos et al. (2007a).
- In "*Step 1*" the fault-induced displacement profile (computed separately with 2-D plane-strain fault rupture propagation analysis) is applied quasi-statically on the tunnel supports.

- At the final "*Step 2*", the model is subjected to dynamic excitation. The ground motion is first "propagated" through the alluvial deposit to take account of soil amplification effects. The resulting ground motion (at seabed) is then applied along the tunnel supports with a time lag.

The reverse situation, i.e. dynamic excitation (Step 2) followed by fault-induced displacement (Step 1), is not reported herein. Ground shaking of the un-deformed structure has been explored in detail in Anastasopoulos et al. (2007a), concluding that the dynamic excitation does not yield significant permanent displacements of the joints. This means that if Step 2 was followed by Step 1, the results would be practically the same with Step 1 analysed alone.

4.1 Soil–tunnel interaction parameters

Even for an embedded tunnel within an idealised elastic medium, the selection of appropriate spring coefficients is not always straight forward. St.John and Zahrah (1987) derived approximate expressions for the spring stiffnesses [expressed as force over displacement per unit length of the tunnel (kN/m/m)], as functions of the incident wavelength. For the two horizontal stiffnesses (x and y), their solution is based on integration of Kelvin's fundamental solution for a "point" load acting within an infinite elastic medium, assumed homogeneous and isotropic. For the vertical spring stiffness (z), they utilised the fundamental solution of a surface-loaded half-space: Flamant's problem (see Poulos and Davis 1974; Davis and Selvadurai 1996). Although with the introduction of wavelength they managed to circumvent the singularity of a plane-strain solution, an additional uncertainty was introduced.

For the problem investigated herein, the adoption of such a solution would not be easily justifiable for the following reasons: (i) Since the tunnel is not embedded, Kelvin's full-space solution is not even approximately applicable; half space solutions can be seen to be more appropriate. (ii) The rigidity of tunnel segments with respect to the near-surface (relatively soft) soil will lead to an almost uniform translation in the horizontal (x or y) direction, rather than sinusoidal deformation; hence, the rigid-foundation solution is more appropriate. (iii) The singularity of the plane-strain solution is "suppressed" due to soil non-homogeneity: the soil modulus is not constant, but increases with depth (Gazetas 1983).

It is therefore reasonable to make use of published elastodynamic solutions for a rigid long rectangular foundation resting on half-space. For the problem investigated herein, the approximate expressions for non-homogeneous half-space proposed by Gazetas (1991) are utilised. Using as a starting point the synthesized generic soil profiles (Anastasopoulos et al. 2007a), the effective shear modulus profile is eventually modeled as:

$$G(z) \approx G_o \left(1 + \alpha \frac{z}{B}\right)^m \tag{1}$$

where G_o is the shear modulus at $z = 0$; $2B$ (=23.5 m) is the width of the tunnel; and α, m soil-model parameters. To take account of soil non-linearity, G_o, α, and m were obtained by curve fitting an equivalent-linear $G = G(z)$ profile (i.e. the profile of the shear modulus in the last iteration of the equivalent-linear wave propagation analysis), rather than the initial $G_{\max}$ profile. The distributed vertical and horizontal springs are then obtained as the *static* vertical, lateral, and axial stiffnesses of a very long tunnel. Expressed as stiffnesses per unit length, the Winkler moduli $\boldsymbol{k}_z, \boldsymbol{k}_y, \boldsymbol{k}_x$, (in kN/m/m) in terms of Poisson's ratio ($\nu \approx 0.50$) are:

$$\boldsymbol{k}_z \approx \frac{0.73}{1-\nu} G_o (1 + 2\alpha)^m \tag{2}$$

$$\boldsymbol{k}_y \approx \frac{2}{2-v} G_o \left(1+\frac{2}{3}\alpha\right)^m \tag{3}$$

$$\boldsymbol{k}_x \approx \boldsymbol{k}_y - \frac{0.2}{0.75-v}\left(1-\frac{B}{L}\right) G_o \left(1+\frac{1}{2}\alpha\right)^m \tag{4}$$

These expressions are considered valid for all frequencies—a reasonable simplification for *translational* modes of vibration (e.g. Gazetas 1991). The effect of embedment is ignored, and "added" indirectly only in the lateral (y) direction (Fig. 6), by increasing the relevant spring coefficient, $\boldsymbol{k}_y$, by the elastic sidewall resistance:

$$\Delta \boldsymbol{k}_y \approx E_{\text{fill}} h/2B \tag{5}$$

where E_{fill}, the (average) Young's modulus of the backfill, and h, the "effective" depth of embedment. This approach bears similarities with the one of Vrettos (2005), whose spring stiffnesses are also independent of wavelength or frequency.

Vertical, $\boldsymbol{c}_z$, lateral, $\boldsymbol{c}_y$, and longitudinal, $\boldsymbol{c}_x$, dashpot coefficients, reflecting hysteretic and radiation damping within the half-space, are obtained similarly (Gazetas 1991). In view of the strong soil in-homogeneity and the relatively low dimensionless frequency parameters, $a_o = (2\pi/T)B/V_{\text{so}}$, that are of prime interest here, these coefficients play a minor role in the response and are not further discussed.

As illustrated in the schematic representation of Fig. 6, in the longitudinal (x) direction the behaviour of the soil-tunnel interface is approximated with a simple slider of friction coefficient μ_x. In the transverse (y) direction, the "interface" is a little more complex, with sliding accompanied by passive type deformation of the backfill. Therefore, the "*equivalent friction coefficient*", μ_y, is estimated through 2-D plane-strain analysis of the tunnel cross-section.

Immersion joints (connecting adjacent tunnel segments) are modeled with non-linear hyper-elastic springs. In the longitudinal (x) direction, the springs simulate the behavior of the Gina gasket. Their hyper-elastic restoring force–deformation backbone curves (Fig. 5) are calibrated with the results of half-size model tests by Kiyomiya (1995). In the transverse (y) and vertical (z) directions such gaskets cannot transfer shear; the drift of one segment relative to the other depends solely on shear-key allowance. Thus, the behavior of the joint is simulated through special "gap" elements. Such elements are initially inactive, becoming very stiff after closure of the gap (i.e. the shear-key allowance), depending mainly on the stiffness of the concrete section in the area of the shear key.

5 Analysis of fault rupture propagation

We first analyse fault rupture propagation through the overlying soil deposit. The location and magnitude of a potential dislocation at the ground surface depend not only on the type and magnitude of the fault rupture, but also on the composition of overlying soils, and the presence of a structure (e.g. Slemmons 1957; Brune and Allen 1967; Berrill 1983; Taylor et al. 1985; Buwalda and St. Amand 1955; Kelson et al. 2001; Sanford 1959; Horsfield 1977; Roth et al. 1981; Cole and Lade 1984; Lade et al. 1984; Bray 1990, 2001; Bray et al. 1994a,b; Lazarte and Bray 1995; Johansson and Konagai 2004; El Nahas et al. 2006). Most importantly, the likelihood of a fault rupture of (vertical) magnitude h to propagate all the way to the ground surface (i.e. at the seabed) through a soil deposit of depth H mainly depends on the bedrock offset ratio h/H and soil ductility (Bray 1990; Cole and Lade 1984; Lade et al. 1984;

Anastasopoulos et al. 2007b). For normal faults and for dip angles α ranging from 45° to 60°, the required h/H for fault outcropping is of the order of 1% (Anastasopoulos et al. 2007b). If h/H does not exceed this critical value, the fault does not outcrop at the ground surface (seabed), and the soil deforms in a more-or-less quasi-elastic manner (Cole and Lade 1984; Lade et al. 1984; Anastasopoulos et al. 2007b). Such deformation can be expected to be much less severe than a distinct fault scarp. The importance of realistic estimation of the maximum probable h/H is evident.

Geotechnical exploration in Rion–Antirrion only reached a maximum depth of 100 m below seabed, without encountering bedrock. To shed more light in the tectonic environment of the area, and to gain better knowledge of the alluvium thickness H, a detailed geophysical investigation (with passive tomography) was conducted (Tselentis et al. 2004), with a network of 70 seismographs capturing seismic waves originating from small magnitude earthquakes. Tomography imaging was used to locate potentially active faults. The main conclusions of the geophysical investigation are as follows:

(i) No seismic activity was detected at depths less than 1.5 km, verifying the hypothesis that faults within the straits do not outcrop *on the seabed*.
(ii) As depicted in Fig. 7a, five rupture zones were detected within the straits, with direction practically perpendicular to the tunnel axis.
(iii) Limestone bedrock ($V_p > 3,500$ m/s) was detected to lie at depths of the order of 800 m (Fig. 7a).

Based on these results, we analyse the central part of the straits down to 800 m depth where "sound" bedrock was detected. The analysis is conducted in plane-strain, with the finite element (FE) code ABAQUS. The FE method has proven successful in analysing fault rupture propagation through soil, provided that certain conditions are satisfied: the use of a refined mesh, a suitable nonlinear constitutive law for the soil, etc. (e.g. Bray et al. 1994a,b). The model is displayed in Fig. 7b. At the $H = 800$ m deep base rock a normal fault of dip angle α ruptures with an offset (downward displacement) of vertical amplitude h. The total width of the model is $B = 4H = 3,200$ m, following the recommendation of Bray (1990). At the central 1,600 m of the model, the discretisation is finer, with the quadrilateral elements being 20 × 20 m (width × height); at the two edges the mesh is coarser (40 × 20 m). The offset is applied to the left part of the model in small consecutive steps.

Based on the findings of a thorough literature review (Anastasopoulos 2005), an elasto-plastic constitutive model with Mohr–Coulomb failure criterion and isotropic strain softening was adopted and encoded in ABAQUS. Such models have been successfully employed in modeling the failure of embankments and cut slopes (Potts et al. 1990, 1997). Strain softening is introduced by reducing the mobilised friction angle φ_{mob} and the mobilised dilation angle ψ_{mob} with the increase of plastic octahedral shear strain:

$$\varphi_{\text{mob}} = \left\{ \begin{array}{ll} \varphi_p - \frac{\varphi_p - \varphi_{\text{res}}}{\gamma_f^P} \gamma_{\text{oct}}^P, & \text{for } 0 \le \gamma_{\text{oct}}^P < \gamma_f^P \\ \varphi_{\text{res}}, & \text{for } \gamma_{\text{oct}}^P \ge \gamma_f^P \end{array} \right\}$$

$$\psi_{\text{mob}} = \left\{ \begin{array}{ll} \psi_p \left(1 - \frac{\gamma_{\text{oct}}^P}{\gamma_f^P} \right), & \text{for } 0 \le \gamma_{\text{oct}}^P < \gamma_f^P \\ 0, & \text{for } \gamma_{\text{oct}}^P \ge \gamma_f^P \end{array} \right\} \tag{6}$$

where φ_p and φ_{res} the peak mobilized friction angle and its residual (or critical state) value; ψ_p the peak dilation angle; γ_f^P the plastic octahedral shear strain at the end of softening. Soil behaviour before yielding is modeled as linear elastic, with a secant modulus G_S increasing

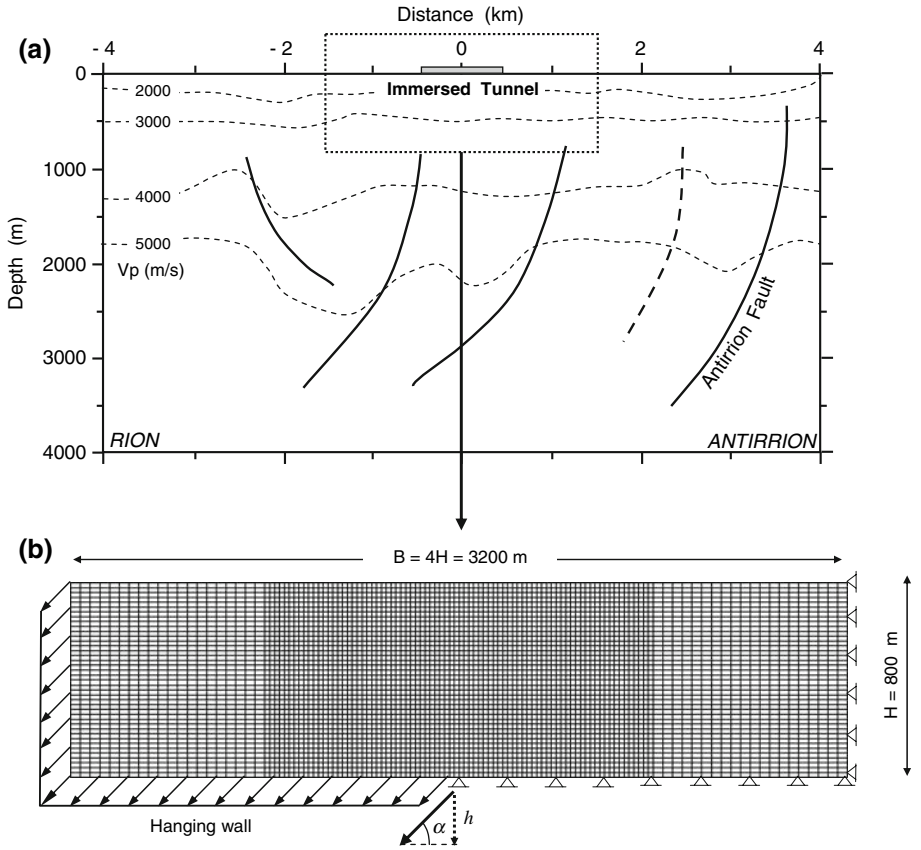

Fig. 7 (**a**) Mapping of active faults in the area of the crossing, based on geophyical tomography (Tselentis 2004), (**b**) Finite element discretization for the plane strain analysis of fault rupture propagation through the 800 m soil sediment

with depth, according to Eq. 1 with $m = 1$. Model parameters are calibrated through direct shear test results, and an approximate scaling method is employed to take account of scale effects, as described in more detail in Anastasopoulos and Gazetas (2007).

The effectiveness of the FE modeling methodology was initially *qualitatively* verified against published case histories (Gilbert 1890; Slemmons 1957; Witkind et al. 1962; Brune and Allen 1967; Stein and Barrientos 1985; Taylor et al. 1985) and experimental results (Horsfield 1977; Cole and Lade 1984). Quantitative validation was provided through successful predictions of centrifuge model tests in sand (Anastasopoulos et al. 2007b).

Given the uncertainties in the soil profile, two idealised soils were parametrically investigated:

(a) dense cohesionless soil: $\varphi_p = 45°$, $\varphi_{\text{res}} = 30°$, $\psi_p = 15°$, $\psi_{\text{res}} = 0°$, and $\gamma_y = 1.5\%$
(b) loose cohesionless soil: $\varphi_p = 30°$, $\varphi_{\text{res}} = 25°$, $\psi_p = 5°$, $\psi_{\text{res}} = 0°$, and $\gamma_y = 3.0\%$

where γ_y is a parameter related to soil ductility. The dense soil reaches "failure" at relatively low strains ("brittle" behaviour), while the loose soil is capable of undertaking larger strains before yielding ("ductile" behaviour).

To be on the conservative side, and despite the more optimistic geophysical results, $h_d = 2\,\text{m}$ was set as the design bedrock offset (vertical component). It is noted that this offset will not necessarily take place during a single seismic event, but may also be the result of aseismic slip accumulation over the years. The dip angle was also conservatively assumed to be $\alpha = 45°$. As already discussed, for small values of h/H the rupture does not reach the seabed. With $H = 800\,\text{m}$, a bedrock offset of 2 m corresponds to $h/H = 0.25\%$. The required h/H for outcropping of the fault rupture is an increasing function of soil ductility, expressed through γ_y. Even for the "brittle" soil with $\gamma_y = 1.5\%$, an h/H in the order of 0.75% is required for the fault to break-out (Anastasopoulos et al. 2007b).

6 Effects of fault rupture on the tunnel

To illustrate the phenomenon, characteristic pictures of the propagating fault rupture through a deposit of an idealised dense sand layer is given in Fig. 8: four snapshots of deformed mesh with superimposed plastic strains, for bedrock displacement h ranging from 1 to 6 m (darker regions denote higher plastic strains). Observe that for bedrock displacements up to $h = 4\,\text{m}$ (i.e. $h/H = 0.50\%$), the rupture does not emerge on the surface (seabed). Only when the imposed bedrock displacement exceeds 6 m (i.e. $h/H = 0.75\%$) does the dislocation (barely) emerge. For the design displacement of 2 m, the rupture is clearly far from reaching the seabed (model surface). The situation is even better with the idealised loose sandy soil.

Figure 9a, b portray the profiles of vertical, Δy, and horizontal displacement, Δx, along the seabed for the (conservative) dense sandy soil and $h_d = 2\,\text{m}$. The horizontal distance, d, is measured from the point of application of the bedrock offset. Figure 9c depicts the slope of the ground surface β, a useful response parameter in assessing the damage potential to overlying structures. The horizontal strain, ε_x, along the ground surface (positive values are for tension) is depicted in Fig. 9d.

Observe that the ground surface deforms smoothly (without a scarp), as the rupture cannot outcrop. The "bending" deformation, expressed through the distortion angle β (Fig. 9c), reaches its peak (0.26%) at $d \approx 200\,\text{m}$. On the other hand, the horizontal (tensile) deformation achieves its maximum value, $\varepsilon_x = 0.25\%$, at distance $d \approx 500\,\text{m}$ (Fig. 9d). The computed displacement profiles (Δx and Δy) are used as the "input" displacement on the tunnel supports. The tensile deformation causes decompression of the joints. The bending deformation de-compresses some of the immersion joints and possibly further compresses

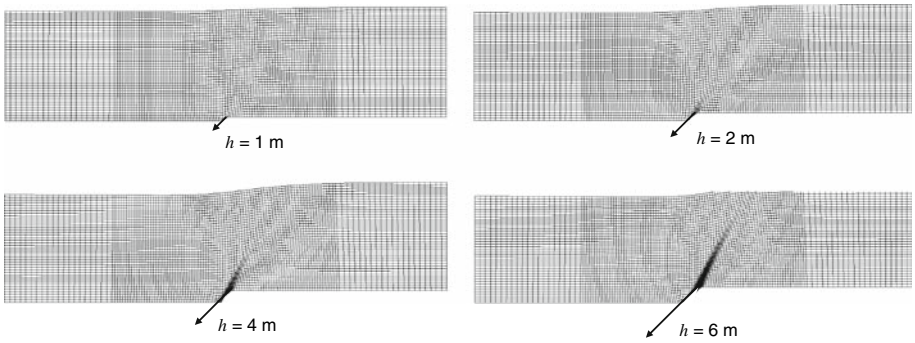

Fig. 8 Snapshots of deformed mesh and plastic strain for a fault rupture $\alpha = 45°$ in dip, and bedrock displacements $h = 1, 2, 4$, and 6 m, for the idealised dense sandy soil

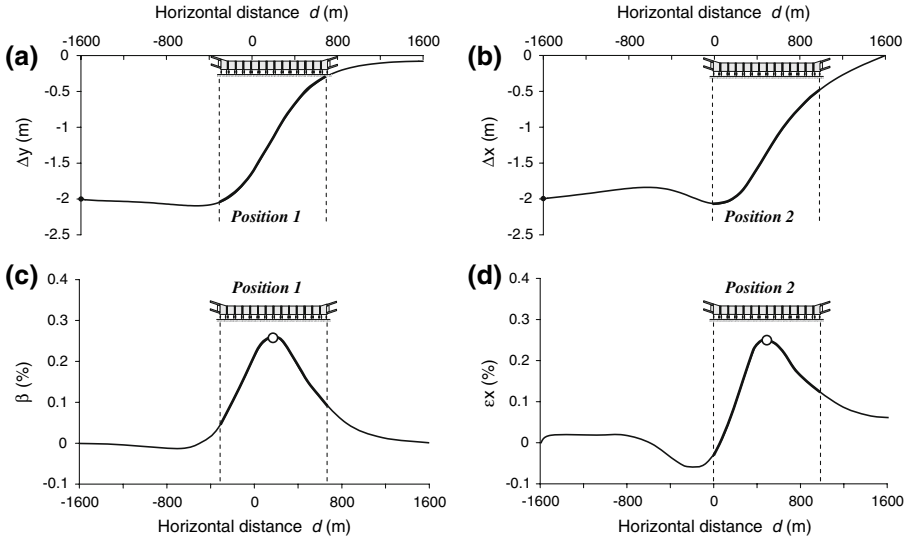

Fig. 9 Rupture propagation analysis results for a fault dipping at $\alpha = 45°$ and bedrock displacement $h_d = 2\,\text{m}$, for the idealised dense sandy soil: (**a**) vertical displacement Δy, (**b**) horizontal displacement Δx, (**c**) angular distortion β, and (**d**) horizontal strain ε_x at the seabed

some other. Since the maximum bending and tensile deformations do not occur in the same location, two tunnel-fault rupture relative positions are identified (Fig. 9):

(1) *Position 1*: the center of the tunnel coincides with the location of max β, and
(2) *Position 2*: the center of the tunnel coincides with the location of max ε_x.

Predicting which is the "worst-case" scenario is not straightforward. Therefore, both positions are investigated.

As depicted in Fig. 10, the normal fault-induced deformation leads to significant decompression of most immersion joints. When the tunnel is at Position 2 relative to the propagating fault rupture (tunnel center at max ε_x), the tectonic deformation leads to decompression of all joints (Fig. 10a, c, d). In contrast, with the tunnel at Position 1 (tunnel center at max β), joints near the left edge of the tunnel (Fig. 10b) are subjected to increased compression due to sagging deformation of the seabed. The thickness of the rubber gasket does not appear to affect substantially the de-compressed profile.

Typical results of a complete analysis are portrayed in Fig. 11, in terms of longitudinal joint deformation δ_x, sliding displacement Δ_x, bending moment M_y, and axial force N. Figure 11a corresponds to segment length $L = 70\,\text{m}$ with type A gasket, while Fig. 11b to $L = 100\,\text{m}$ with type B gasket. While $L = 165\,\text{m}$ was also examined, the results are not shown herein: with such a large length the tunnel cannot sustain the total distress without several joints experiencing net tension—a precarious situation indeed. Similarly, the "allowance" in the shear-keys plays only a minor role; thus, results are given only for a single value (5 mm) of this "allowance". In all cases, the presented results correspond to the position "2" scenario, which proved to be critical.

The following conclusions are drawn:

1. The application of the fault-induced tensile displacement de-compresses all the joints. The de-compression (δ_x) is largest near the middle of the tunnel, and is more pronounced when the segment length is 100 m.

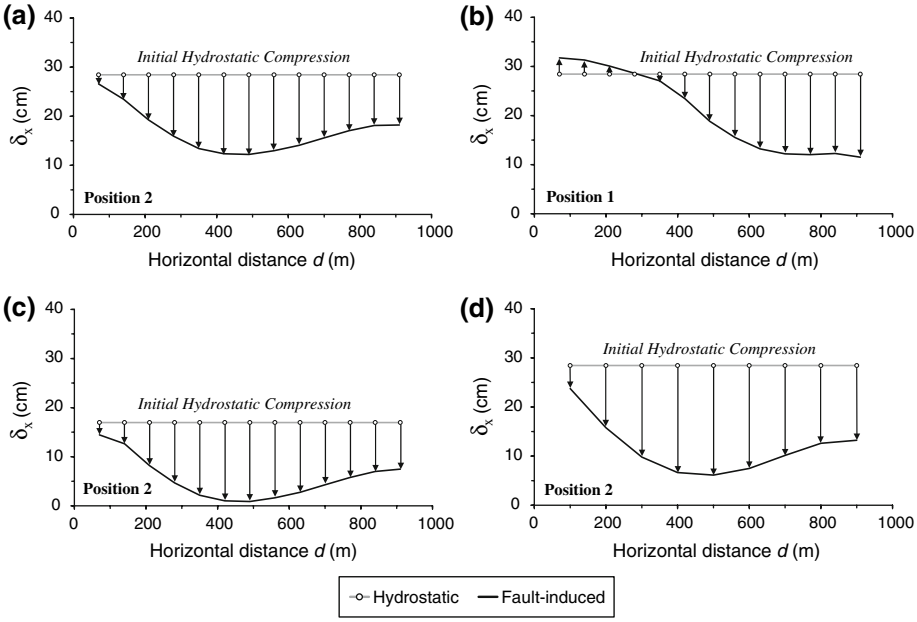

Fig. 10 Fault-induced decompression of the immersion joints, starting from the initial hydrostatic compression: (**a**) 70 m segments with Type B gasket, at Position 2 (max tensile displacement), (**b**) 70 m segments with Type B gasket, at Position 1 (max bending displacement), (**c**) 70 m segments with Type A gasket, at Position 2, and (**d**) 100 m segments with Type B gasket, at Position 2

2. The initial slippage Δ_x is greater near the middle of the tunnel, where the maximum tensile deformation ε_x takes place. Increasing the segment length only marginally increases the maximum sliding displacement.
3. At first, the axial force (N) exhibits an initial hydrostatic "pre-stressing" of 160 MN (Step 0). Then, application of the fault-induced deformation (Step 1) causes longitudinal decompression of the tunnel, reducing N significantly. For the 70 m segments, N drops from 160 MN to barely 30 MN near the middle. The increase of segment length makes things worse: the initial compression is completely lost, and even some (small) tensile stressing develops (at point "C").

7 Methodology of dynamic analysis

Figure 12 illustrates schematically the methodology of dynamic analysis. In a first sub-step, the ground motion is applied at the bedrock and "propagated" through the soil deposit to compute the free-field (i.e. ignoring soil–structure interaction) ground motion at the seabed. The latter is then applied to the already deformed (due to fault-induced deformation) tunnel supports (springs and dashpots), as described in the sequel.

Free-field acceleration time histories are computed trough 1-D wave propagation analysis, conducted with two methods: (i) making use of the widely accepted equivalent linear approximation—code SHAKE (Schnabel et al. 1972), and (ii) applying the nonlinear constitutive model "BWGG", developed by Gerolymos and Gazetas (2005) and encoded in the numerical code NL-DYAS. While the first method is most popular, it has certain limitations,

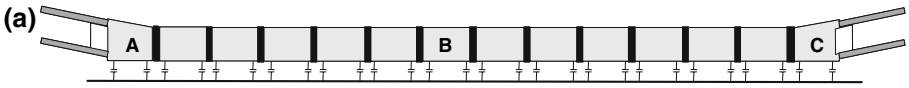

70 m segment length – Type A gasket				
	Joint Decompression δ_x (cm)	Segment Slippage Δ_x (cm)	Axial Force N (MN)	Bending Moment M_y (MNm)
A	1	0	-130	-70
B	16	7.5	-30	40
C	10	5	-50	5

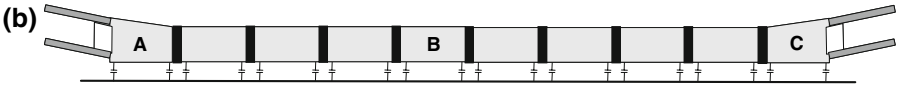

100 m segment length – Type B gasket				
	Joint Decompression δ_x (cm)	Segment Slippage Δ_x (cm)	Axial Force N (MN)	Bending Moment M_y (MNm)
A	4	1	-100	-150
B	21	-9	-80	-10
C	14	-2	10	140

Fig. 11 Joint deformation, sliding displacement, axial forces and bending moments due to fault-induced deformation for (**a**) 70 m segments and (**b**) 100 m segments. Fault at Position 2, type B gasket, and 5 mm shear-key allowance

especially in the case of very deep soil deposits (as in our case). Such disadvantages can be overcome with NL-DYAS, which is capable of reproducing even some of the most complex non-linear characteristics of cyclic behavior, such as cyclic mobility and liquefaction. More details on the 1-D wave propagation analysis can be found in Anastasopoulos et al. (2007a).

The computed free-field time histories are then applied to tunnel supports, but not simultaneously. For long structures, the ground motion differs from one support to another: in the arrival time, in amplitude, and in frequency content. Such variations are due to: (a) the "wave passage" effect (seismic waves do not propagate only vertically), (b) local soil conditions (variation of the soil profile along the alignment), and (c) random "geometric" incoherence (due to reflections, refractions, and superposition of incident seismic waves stemming from random ground heterogeneities). An elaborate review on the subject has been published by Hashash et al. (2001).

To take account of the "wave passage" effect, the computed free-field acceleration time histories are applied on tunnel supports (springs and dashpots) with a time lag, following the methodology of EC8—Part 2 (2002). At distance x_i along the axis of the tunnel, the seismic excitation will arrive with a time lag (Fig. 12):

$$t_i = x_i / C_\alpha \tag{7}$$

Vertically propagating seismic shear waves would appear traveling along the ground surface (the seabed) with $C_\alpha \to \infty$. Waves propagating at incidence angle $\beta_s \neq 0°$ from the vertical, appear traveling with finite C_α:

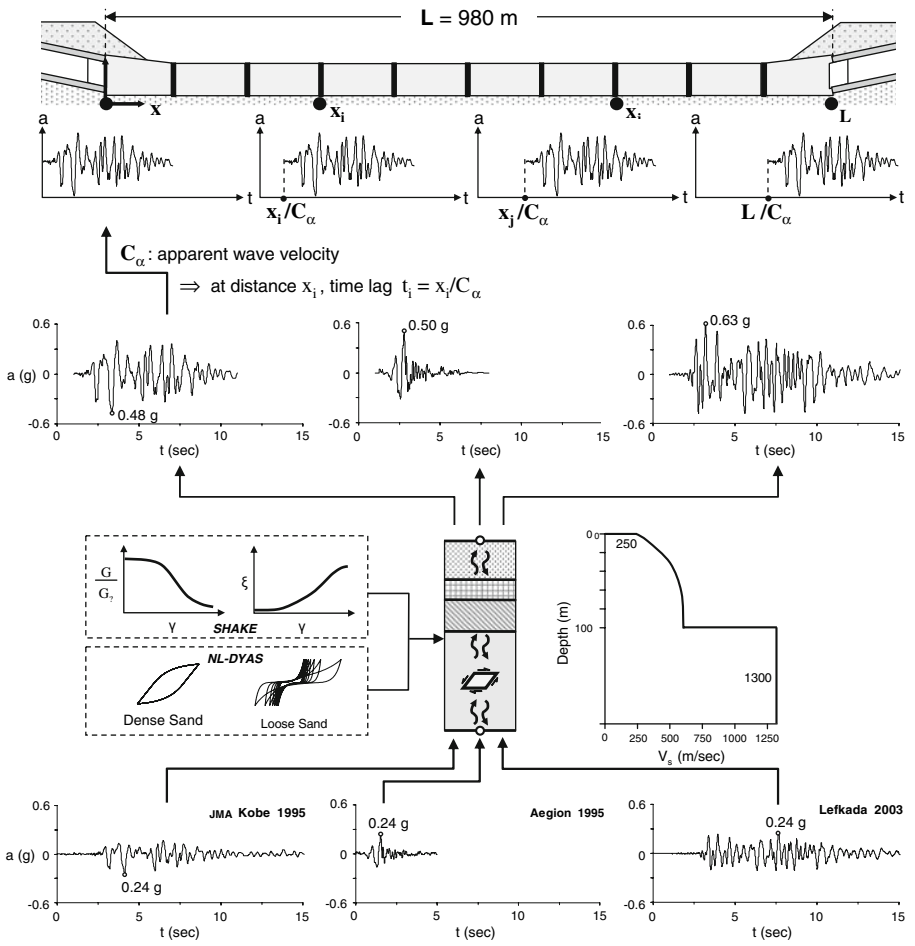

Fig. 12 Dynamic analysis methodology and results for the worst-case scenario ("stiff" soil profile with $V_s = 1,300$ m/s below 100 m depth). The bedrock acceleration excites the 1-D soil column; wave propagation is analysed alternatively with the equivalent linear method (SHAKE) and the truly nonlinear code NL-DYAS to derive the acceleration at the seabed (characteristic such time histories are shown). Then, the acceleration time histories are imposed with a time lag on the spring-dashpot supports of the tunnel

$$C_\alpha = V_s / \sin \beta_s \tag{8}$$

where V_s is the shear wave velocity of the soil near the surface. β_s depends on the distance to the source and the ray path, but also and crucially on the shear wave velocity contrast between the near-surface soil layers and the underlying ground: larger contrast increases the refraction of seismic waves, decreasing β_s, thanks to Snell's law.

Field records in Japan have shown that C_α may range from 1,000 to 2,000 m/s (Kiyomiya 1995; Okamoto 1984). For the 1971 San Fernando and the 1979 Imperial Valley earthquakes, O'Rourke et al. (1982) estimated C_α to range from 2,100 to 5,300 m/s. Following the recommendations of EC8—Part 2 (2002), and to be on the conservative side, we assume $C_\alpha = 1,000$ m/s.

Regarding local soil conditions, the soil is assumed to be uniform along the tunnel: a reasonable simplification at this stage of knowledge. The effect of geometric incoherence was investigated in the early stages of the study applying both the coherency loss functions of Abrahamson et al. (1991), and the theoretical coherency loss model of Luco and Wong (1986). The effect of such incoherence was found to be insignificant compared to the wave passage effect, especially in view of the conservative choice of $C_\alpha = 1,000$ m/s.

7.1 Analysis of soil response

Consistently with the Greek Seismic Code (EAK 2000) we selected $A = 0.24$ g for the basement excitation. Four real earthquake records were selected and downscaled for analysis (Table 1): (a) the JMA record of the 1995 M_{JMA} 7.2 Kobe earthquake (Fukushima et al. 2000); (b) the Rinaldi record of the 1994 Northridge M_s 6.8 earthquake (Trifunac et al. 1998); (c) the record of the 1995 Aegion M_s 6.2 earthquake (Gazetas 1996); and (d) the record of the 2003 Lefkada M_s 6.4 earthquake (Gazetas et al. 2005; Benetatos et al. 2005). This ensemble of ground motions ensures that the excitation is rich in long periods and strong pulses (a critical parameter for inelastic systems), and that near-fault effects are taken into account. More details on the seismic environment and the selection and scaling of the ground motions can be found in Anastasopoulos et al. (2007a).

Figure 12 illustrates 1-D wave propagation results for three of the records and for one of the worse-case scenarios: "stiff" soil profile with $V_s = 1,300$ m/s below 100 m depth. The Aegion and the Kobe JMA records produce peak ground acceleration (PGA) in the order of 0.50 g at the seabed, while the Lefkada accelerogram yields 0.63 g. Five more possible soil profiles were parametrically investigated. From all of the examined soil profile and seismic excitation scenarios, PGA and PGVs were found to range between 0.40 and 0.63 g and 0.42 and 0.81 m/s, respectively (Table 1).

8 Combined effects of fault rupture and subsequent seismic shaking

Typical results of a complete analysis are portrayed in Figs. 13–16, in the form of time histories of longitudinal accelerations (a_x), axial forces (N), longitudinal sliding displacements (Δ_x), and axial joint deformations (δ_x), which develop at various "points" along the tunnel during strong seismic shaking. Quasi-static deformation and "distress" is assumed to have already taken place in a preceding event of fault rupturing underneath the site of the tunnel (Step 1).

Each of these figures presents results for two different values of segment length L: 70 and 100 m. Results for $L = 165$ m are not shown: with such a large length the tunnel would not be able to sustain the total developing stressing without several joints experiencing net tension—a precarious situation indeed. Only results for the (scaled-down) Kobe JMA excitation are shown in these figures, since the other motions lead to a qualitatively similar behaviour, and the conclusions drawn herein are not altered. The "allowance" in the shear-keys proved to play only a minor role; thus, results are given only for a single value (5 mm). Finally, only the most critical location of the emerging fault rupture, position "2", is examined here.

Figure 13 depicts the time histories of longitudinal acceleration a_x which develop in the middle of three characteristic tunnel segments (B, C, and D), and contrasts them with the ground (seabed) excitation (point A). Observe that the response of the tunnel differs from point to point. The peak acceleration is amplified from 0.48 g at the base to approximately 0.60 g near the terminal segments (at the two edges of the tunnel, B and D). Near the center, however, the (longitudinal) acceleration is cut-off to about 0.30 g, implying sliding. This

Table 1 Strong motion records used in the analysis

Record:	Record data			Original		Scaled[c]		Seabed[d]	
	M_s	E-dist[a] (km)	F-dist[b] (km)	PGA (g)	PGV (cm/s)	PGA (g)	PGV (cm/s)	PGA (g)	PGV (cm/s)
Kobe JMA	7.2	22	1.5	0.82	81	0.24	24	0.48	64
Rinaldi	6.8	9	2	0.79	164	0.24	50	0.53	81
Aegion 1995	6.2	11	4	0.54	52	0.24	23	0.50	48
Lefkada 2003	6.4	14	14	0.43	33	0.24	18	0.63	42

[a] Epicentral distance
[b] Distance to fault
[c] Input for 1-D soil response analysis
[d] Output from 1-D soil response analysis, used as input to the tunnel-soil model

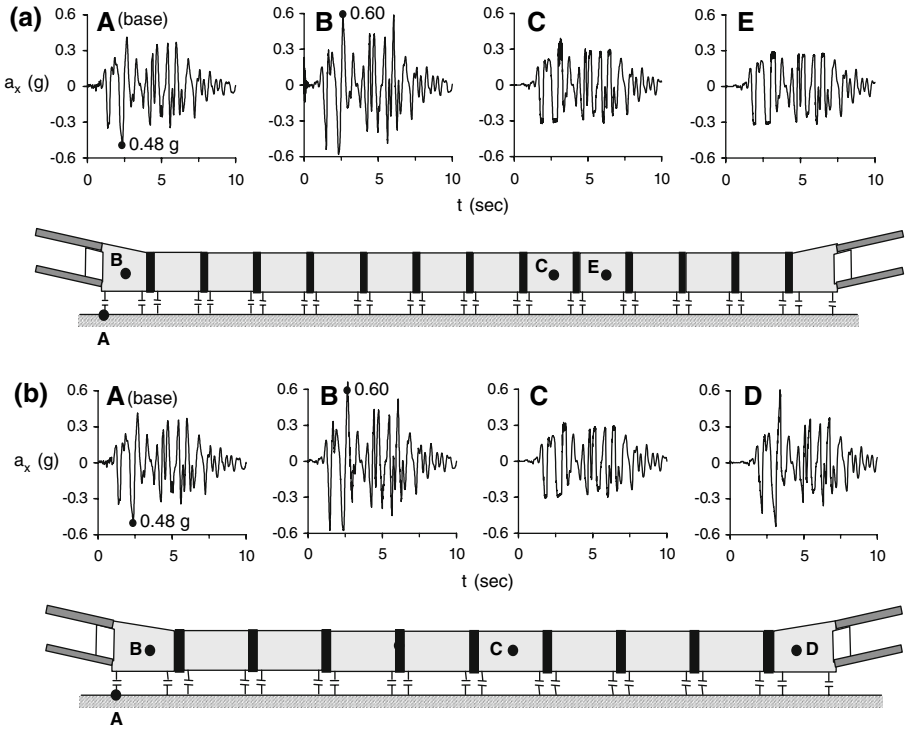

Fig. 13 Longitudinal acceleration time histories for: (**a**) 70 m segments and (**b**) 100 m segments. (Kobe JMA excitation, fault at Position 2, type B gasket, and 5 mm shear-key allowance)

differential longitudinal response is attributed to the non-uniform (along the axis) fault-induced displacement and the ensuing tendency of the (spring-restrained) tunnel segments to "readjust" under the subsequent dynamic loading. This is explained in detail in the next section. If the fault-induced displacement did not pre-exist (Step 1), the dynamic response of the tunnel would be nearly uniform (Anastasopoulos et al. 2007a). The increase of L does not appear to have a significant effect on such accelerations.

The sliding displacement Δ_x of tunnel segments is seen in Fig. 14. In the examined direction (x), the tunnel segments have already slipped before application of the asynchronous dynamic excitation (Step 2), due to the fault-induced longitudinal deformation (Step 1). This initial slippage is greater near the middle of the tunnel, where the maximum tensile deformation ε_x takes place, and increases with segment length (from 7 cm for $L = 70$ m, to about 11 cm $L = 100$ m). The increase of L also leads to increased additional dynamic relative displacements. While for $L = 70$ m the additional sliding due to the dynamic excitation reaches 10 cm, for $L = 100$ m the maximum relative dynamic displacement exceeds 16 cm (location B). In all cases, the residual slippage is invariably significantly lower than the maximum value.

Figure 15 illustrates the axial forces N in characteristic cross-sections of the immersed tunnel. At first, the axial force exhibits the initial hydrostatic "pre-stressing" of about 160 MN (Step 0). Then, the application of the fault-induced deformation (Step 1) causes longitudinal decompression of the tunnel, reducing the axial force (N) significantly. The re-adjustment of the segments during dynamic shaking (further explained in the sequel), leads to a

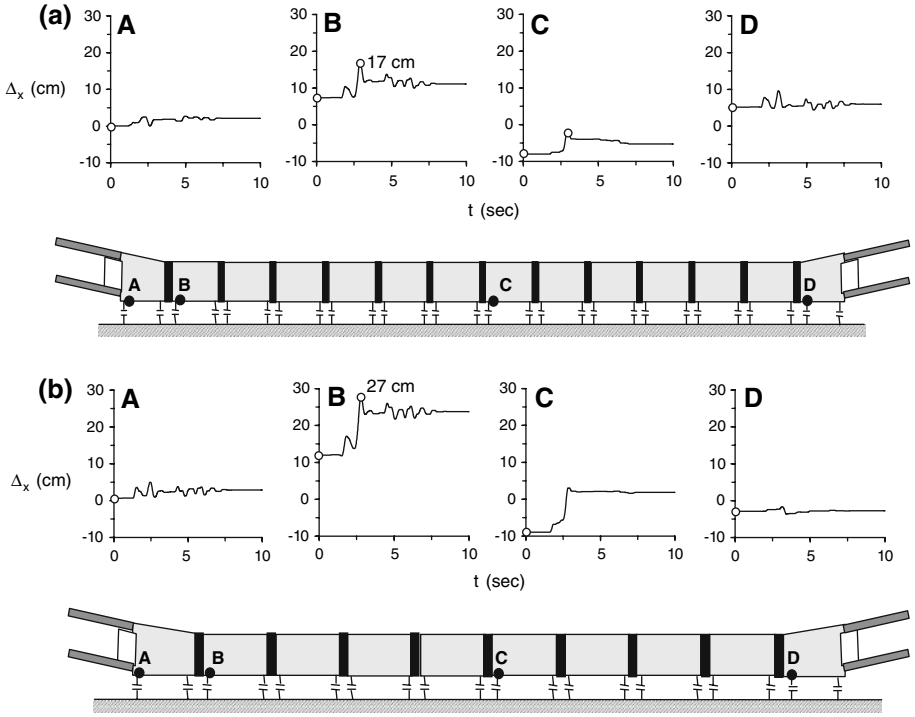

Fig. 14 Longitudinal sliding displacements for: (**a**) 70 m segments and (**b**) 100 m segments. (Kobe JMA excitation, fault at Position 2, Type B gasket, and 5 mm shear-key allowance)

re-distribution of the longitudinal axial force. Segments with higher axial forces tend to get un-loaded, while those subjected to tension (smaller compression) tend to attract higher compression. At the end of shaking, this re-distribution leads to a nearly uniform distribution of the axial force: about 70 MN for $L = 70$ m, and 60 MN for $L = 100$ m. In the latter case, a maximum net tension of about -10 MN is observed during shaking.

The longitudinal deformation (δ_x) of the immersion joints is perhaps the most crucial response parameter for the seismic safety of an immersed tunnel. Their time histories during seismic shaking, and after the fault rupture has already had its effect, are portrayed in Fig. 16, for the 70 m-segment tunnel. We compare the response of the tunnel equipped with the Type A gasket, versus Type B gasket. Notice that in the longitudinal direction, the Gina gasket experiences an initial hydrostatic compression (Step 0) of 17 and 28 cm, for Type A and B gasket, respectively (Fig. 10). The previous application of the fault-induced tensile displacement opens-up all the joints, with those near the middle of the tunnel experiencing the greatest tension (see also Fig. 10). For Type A gasket, the 17 cm of hydrostatic compression are practically completely lost at the central part of the tunnel (point C), where the remaining compression amounts to a mere 2 cm. The situation near the terminal segments A and D is less critical, with the remaining compression of the gasket being 15 and 6 cm, respectively. During subsequent seismic shaking, the gaskets experience alternating cycles of de-compression and re-compression. While the dynamic compression is acceptably small, there is some tensile deformation in gaskets A and C—a rather precarious situation.

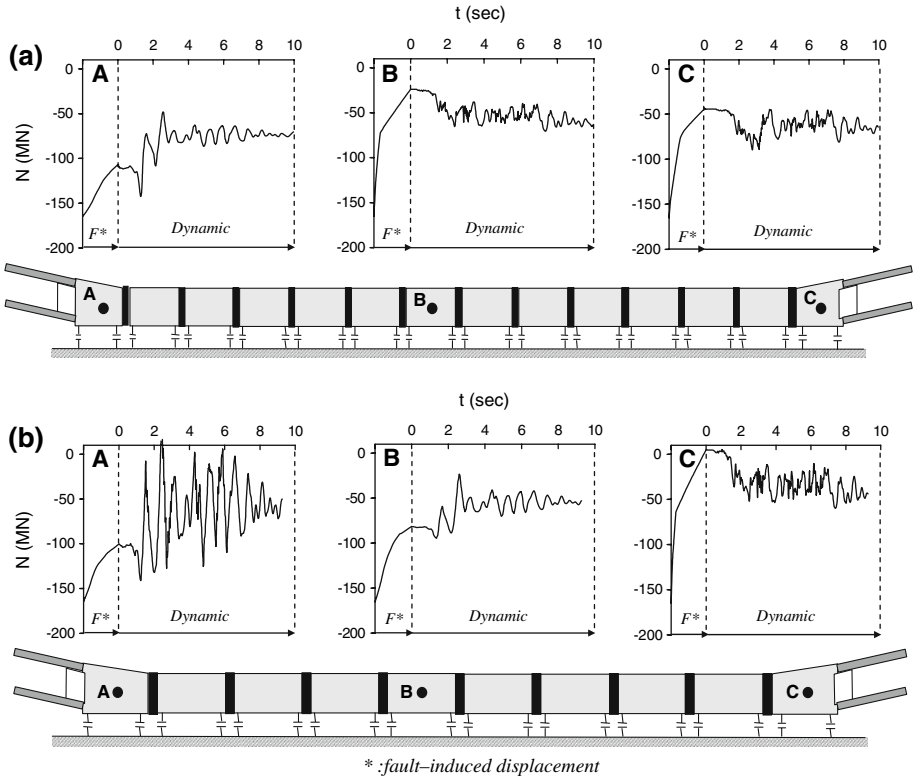

Fig. 15 Axial force and bending moment time histories for: (**a**) 70 m segments and (**b**) 100 m segments (Kobe JMA excitation, fault at Position 2, type B gasket, and 5 mm shear-key allowance)

The use of Type B rubber gasket improves the performance substantially. One of the reasons, of course, is the 28 cm of initial hydrostatic compression. Much greater margins for de-compression are thus available. The fault-induced de-compression of the joints still leaves a respectable minimum compression of 12 cm in the critical central part of the tunnel (point C). As expected, the largest decompression is observed at joints near the middle of the tunnel, where the fault-induced tensile deformation of the seabed is maximum; near the end segments unloading of gaskets is substantially less. During seismic oscillation, the rubber gaskets experience cycles of de-compression and re-compression. The total dynamic-plus-static compression does not, in any case, exceed the acceptable limits of the Type B gasket: $\delta_{x,\max} \approx 29$ cm. More importantly, the gasket remains always compressed, maintaining its water-tightness: $\delta_{x,\min} > 10$ cm, in all joints. A re-distribution of joint deformation is readily observed: *over*-stressed joints tend to *de*-compress, *under*-stressed to *re*-compress, so that the safety of the immersed tunnel improves after strong seismic shaking.

This is a fundamental conclusion, observed in all the parametric cases. Moreover, it is completely explainable theoretically. Its practical significance and its generality should not be underestimated: a detrimental static de-compression of a few of the joints (arising from a rupturing fault, or perhaps from differential settlements, or from any other cause) may be relaxed due to the tunnel oscillations during a strong seismic shaking!

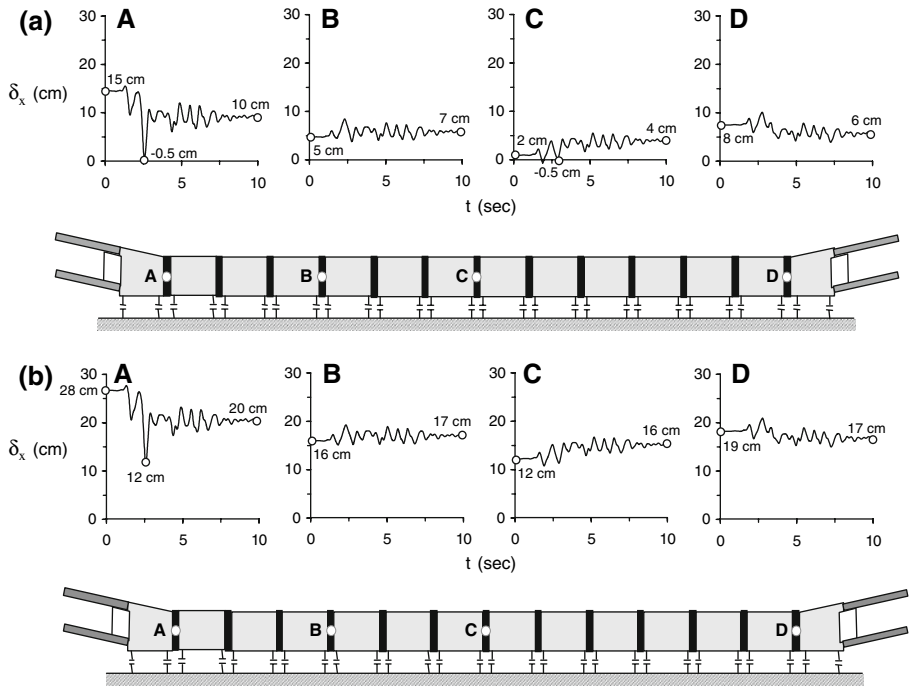

Fig. 16 Longitudinal joint deformation for: (**a**) 70 m segments with Type A gasket and (**b**) 70 m segments with Type B gasket (Kobe JMA excitation, fault at Position 2, and 5 mm shear-key allowance)

9 Dynamic re-adjustment of tunnel segments: a "Healing" process

As already cited, during the asynchronous dynamic oscillation of the tunnel, a redistribution of total deformation among joints is observed. This section sheds further light into this interesting phenomenon.

As depicted in Fig. 17, the application of the fault-induced deformation leads to de-compression of the immersion joints. When the tunnel is at *Position* 2 relative to the propagating fault rupture (tunnel center coinciding with the location of maximum ε_x), the tectonic deformation leads to de-compression of all joints (Fig. 17a, c, d). On the other hand, when the tunnel is placed at *Position* 1 relative to the fault rupture (center of the tunnel coinciding with the location of max. β), most joints de-compress, except those near the left edge of the tunnel (Fig. 17b). At this location, the sagging deformation of the seabed seems to be the most important, imposing some further compression onto the joints. More specifically, in the case of the 70 m segment tunnel with the ("thick") Type B rubber gaskets at *Position* 2 (Fig. 17a), the joints de-compress from their initial hydrostatic compression of 28 cm to a minimum of 12 cm (a de-compression of 16 cm) near the center of the tunnel (where maximum tensile deformation occurs). This de-compression is reduced significantly near the left edge of the tunnel ($\delta_x \approx 26$ cm), but not to the same extent at the right ($\delta_x \approx 18$ cm).

As shown in Fig. 17c, the thickness of the rubber gasket does not substantially affect the de-compressed profile. But while the de-compression is practically the same, in the case of the (slimmer) Type A rubber gasket, the initial hydrostatic compression is only 18 cm. As a result, the joints near the center almost loose all of their pre-stressing ($\delta_x \approx 2$ cm). This

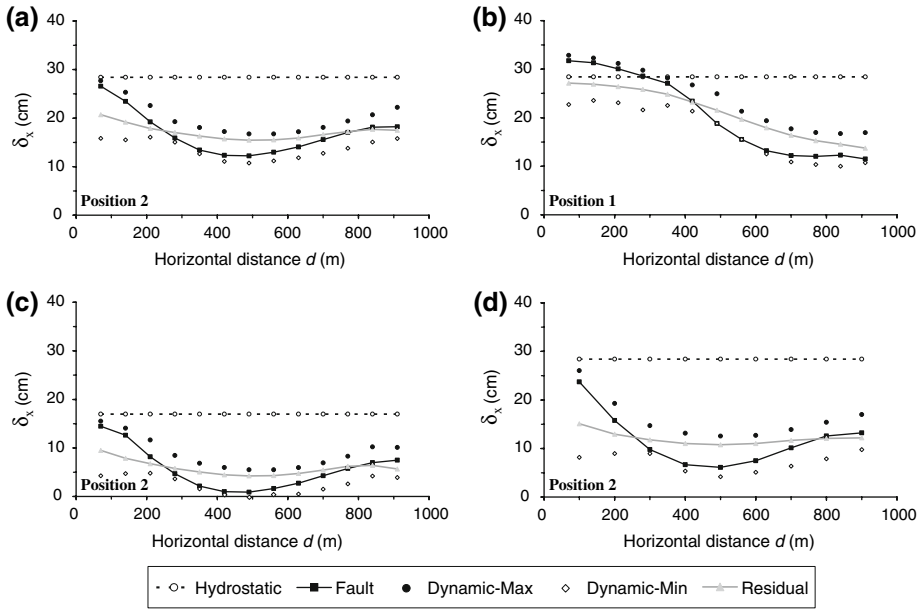

Fig. 17 Dynamic redistribution of the immersion joint deformation: (**a**) 70 m segments with Type B gasket, at Position 2 (max tensile displacement), (**b**) 70 m segments with Type B gasket, at Position 1 (max bending displacement), (**c**) 70 m segments with Type A gasket, at Position 2, and (**d**) 100 m segments with Type B gasket, at Position 2

is threatening for the water-tightness of the tunnel. Increasing L to 100 m (combined with a Type B gasket) improves the safety margins: $\delta_{x,\min} \approx 6$ cm near the center of the tunnel (Fig. 17d). This effect can be easily explained: while for $L = 70$ m the imposed deformation is "absorbed" by a total of 13 joints, in the case of the 100 m segments the same deformation is transmitted to only nine joints. Obviously, this decrease in the number of joints unavoidably increases the "opening" of each joint. Observe that the total de-compression (of all joints) remains practically the same: $\delta_{x,\text{total}} \approx 1.5$ m.

An insight into the aforementioned dynamic re-adjustment of the tunnel segments can be developed with the help of Fig. 18, which illustrates the "history" of longitudinal deformations of six characteristic (Type B) joints along the 70 m segment tunnel, subjected to fault rupturing at *Position* 2. Initially, when only the hydrostatic compression has been applied (Step 0), all joints are compressed by exactly the same amount, reaching $\delta_x \approx 28$ cm.

Application of the fault-induced dislocation (Step 1) leads to a differential de-compression of the joints, as already explained in Fig. 17. At Step 2, the dynamic oscillation tends to re-distribute the joint compressions and relocate the tunnel segments. Observe that joint 1, which had experienced the *least* de-compression, now experiences the *greatest* de-compression during dynamic oscillation. On the contrary, joint 7 at the center of the tunnel, with the *largest* fault-induced *de*-compression, is *re*-compressed the most during shaking.

This surprisingly favorable performance is attributable to the hyper-elastic behaviour of the immersion joints, combined with the "ability" of the tunnel segments to slide over the seabed. Let us now look into the performance of joints 1 and 7 in more detail. As depicted in Fig. 18, the fault-induced stressing only slightly de-compresses the rubber gasket of joint 1 (from 28 to 26 cm): point a_1 in the graph. At the same time (Step 1), joint 7 is significantly de-compressed

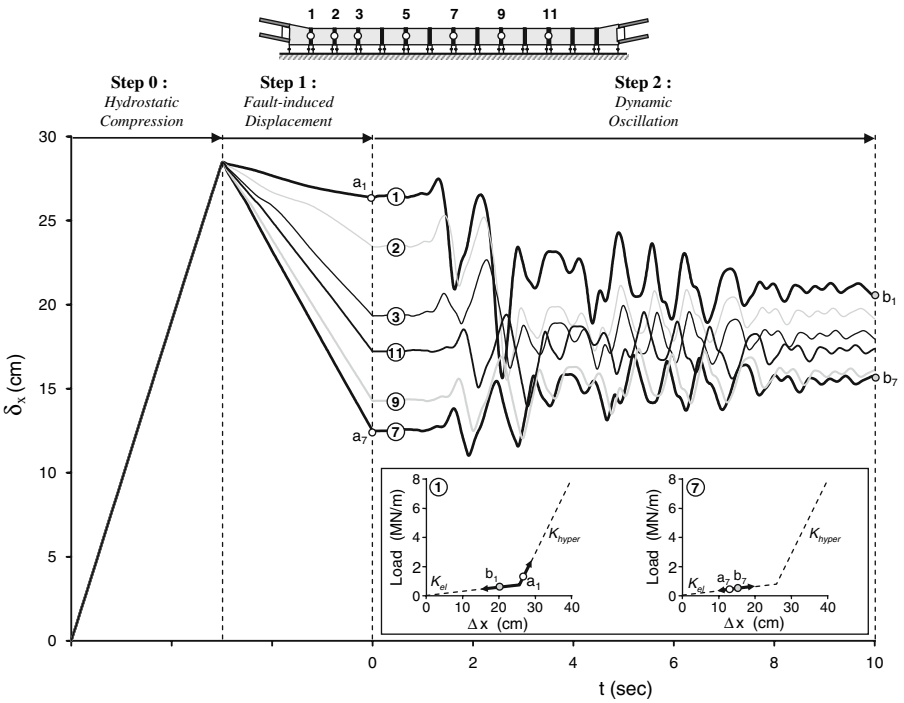

Fig. 18 Longitudinal joint deformation for the 70 m segment tunnel, equipped with the "thick" Type B rubber gasket, and 5 mm shear-key allowance, at Position 2 (maximum tensile deformation) relative to the fault rupture. While the fault-induced displacement in Step 1 "opens" the joints, the asynchronous dynamic shaking tends to relocate the segments and allow for a redistribution of the gasket deformations: observe the substantial homogenization of the residual compression of the joints

to 12 cm: point a_7 in the graph. Now look into the hyper-elastic load-deformation curves of the two joints (see also Fig. 5). Joint 1, after application of the fault-induced displacement remains sufficiently compressed to lie on the stiffer hyper-elastic regime, where the stiffness is $K_{\text{hyper}} \approx 50$ MPa. In stark contrast, joint 7, having de-compressed significantly, lies on the initial soft (elastic) branch, of $K_{\text{el}} \approx 3$ MPa. As a result, during dynamic shaking, joint 1 will be an order of magnitude stiffer than joint 7! Since the joints are connected in series, the stiffer ones simply force the softer to compress. In other words, *over*-compressed joints (*stiffer*) force the *under*-compressed joints (*softer)* to *re*-compress. Of course, such a re-compression leads in turn to hyper-elastic stiffening, making the latter stiffer. Finally, an "equilibrium" is reached, with all joint compressions being substantially "homogenised". At the end of shaking, the stiffer joint 1 exhibits a residual de-compression $\delta_x \approx 20$ cm (point b_1 in the graph), while the softer joint 7 is re-compressed to $\delta_x \approx 13$ cm (point b_7). It must be pointed out that such a behaviour would hardly be possible if it were not for tunnel sliding: if the segments were "fixed" on the seabed, the stiffness of the joints would play no, or very minor, role.

10 Conclusions

Several conclusions of practical significance can be drawn from the presented study (and some additional parametric results not shown here for the sake of brevity):

(1) A properly designed immersed tunnel (suitable thick elastic gaskets; relatively small segment length; shear keys with sufficient "allowance"; un-stressed tendons) can safely resist:
   - a normal earthquake fault rupture with a dislocation (offset) of 2 m in the basement rock, 800 m underneath the tunnel
   - a subsequent strong ground shaking arising from a different significant seismic fault not crossing the site, but producing peak acceleration of at least 0.50 g
   - the cumulative effect of the above two events, even in the worst possible sequence: fault rupture followed by shaking.

(2) The initial hydrostatic compressive force is independent of segment length, or of total number of joints. Increasing the total number of the joints (or decreasing segment length) leads to increased total initial hydrostatic compressive deformation of the tunnel. The initial compression of the Gina gaskets must be large to ensure its water-tightness by avoiding net tension, but strong enough to avoid lateral tensile rupture.

(3) The dynamically-induced longitudinal deformation of the immersion joints depends on segment length L and the thickness of the Gina gasket. Increasing L unavoidably increases both the fault-induced and the dynamic deformation of the immersion joints. Since the tunnel segments are significantly stiffer than the Gina gaskets, they tend to behave as rigid blocks and most of the imposed deformation is "absorbed" in the joints. Obviously, decreasing the number of joints, increases their deformation.

(4) Increasing the thickness of the Gina gasket leads to greater initial hydrostatic compression: from 17 cm for the Type A gasket, to 29 cm for Type B. Since the tectonic deformation is mainly tensile, this increase of the initial compressive deformation leads to higher safety margins. During seismic shaking, the dynamic re-compression and de-compression of the joints is not that sensitive to gasket thickness.

(5) During subsequent (asynchronous) dynamic shaking, the tunnel segments tend to re-adjust by sliding longitudinally over the seabed. This is accompanied by a redistribution of the longitudinal joint deformation leading to a more uniform profile of compression along the length. This surprising "healing" behaviour is attributable (to a substantial extent) to the hyper-elasticity of the rubber gaskets, combined with the "capability" of the segments to slide on the seabed. Thus, while the fault displacements lead to a detrimental de-compression different from joint to joint, upon subsequent seismic shaking the most seriously de-compressed joints become more flexible compared to joints with minor de-compression. Since the joints are connected in series, the stiffer ones will force the softer to re-compress—a beneficial effect of great significance.

Although this research was prompted by the needs of a specific engineering project, the methods of analysis, the proposed design concepts, and hopefully many of the conclusions of this study are sufficiently general to be applicable in other immersed tunneling projects.

Acknowledgements The authors would like to acknowledge the financing of this research project by the Greek Railway Organization (OSE). We acknowledge the invaluable help over the years from Dr. Takashi Tazoh of the Institute of Technology, Shimizu Corporation, Japan.

References

ABAQUS, Inc. (2004) ABAQUS V.6.4 User's manual. Providence, Rhode Island, USA

Abrahamson NA, Schneider JF, Stepp JC (1991) Empirical spatial coherency functions for soil–structure interaction analyses. Earthquake Spectra 7(1):1–27

Anastasopoulos I (2005) Fault rupture–soil–foundation–structure interaction. Ph.D. Dissertation, School of Civil Engineering, National Technical University, Athens, pp 570

Anastasopoulos I, Gazetas G (2007) Behaviour of structure–foundation systems over a rupturing normal fault: II. Analyses, experiments, and the Kocaeli case histories. Bull Earthquake Eng 5(3):277–301

Anastasopoulos I, Gerolymos N, Drosos V, Kourkoulis R, Georgarakos T, Gazetas G (2007a) Nonlinear response of deep immersed tunnel to strong seismic shaking. J Geotech Geoenviron Eng ASCE 133(9):1067–1090

Anastasopoulos I, Gazetas G, Bransby MF, Davies MCR, El Nahas A (2007b) Fault rupture propagation through sand: finite element analysis and validation through centrifuge experiments. J Geotech Geoenviron Eng ASCE 133(8):943–958

Benetatos C, Kiratzi A, Roumelioti Z, Stavrakakis G, Drakatos G, Latoussakis I (2005) The 14 August 2003 Lefkada Island (Greece) earthquake: focal mechanisms of the mainshock and of the aftershock sequence. J Seismol 9(2):171–190

Bernard P et al (1997) The $M_S = 6.2$, June 15, 1995 Aigion Earthquake (Greece): evidence for a low-angle normal faulting in the Corinth rift. J Seismol 1:131–150

Berrill JB (1983) Two-dimensional analysis of the effect of fault rupture on buildings with shallow foundations. Soil Dyn Earthquake Eng 2(3):156–160

Bickel JO, Tanner DN (1982) Sunken tube tunnels In: Bickel JO, Keusel TR (eds) Tunnel engineering handbook, Chap. 13. Van Nostrand Reinholds, pp 354–394

Bray JD (1990) The effects of tectonic movements on stresses and deformations in earth embankments. Ph.D. Dissertation, University of California, Berkeley

Bray JD (2001) Developing mitigation measures for the hazards associated with earthquake surface fault rupture. In: A workshop on seismic fault-induced failures—possible remedies for damage to urban facilities. Japan Society for the Promotion of Science, University of Tokyo, Japan, January 11–12, pp 55–79

Bray JD, Seed RB, Cluff LS, Seed HB (1994a) Earthquake fault rupture propagation through soil. J Geotech Eng ASCE 120(3):543–561

Bray JD, Seed RB, Seed HB (1994b) Analysis of earthquake fault rupture propagation through cohesive soil. J Geotech Eng ASCE 120(3):562–580

Brune JN, Allen CR (1967) A low-stress-drop, low magnitude earthquake with surface faulting. The Imperial, California, Earthquake of March 4, 1966. Bull Seismol Soc Am 57:501–514

Buwalda JP, St. Amand P (1955) Geological effects of the Arvin-Tehachapi Earthquake, California Division of Mines. Bulletin 171:41–56

Cole DA, Jr., Lade PV (1984) Influence zones in alluvium over dip-slip faults. J Geotech Eng ASCE 110(5):599–615

Davis RO, Selvadurai APS (1996) Elasticity and geomechanics. Cambridge University Press

Douglas WS, Warshaw R (1971) Design of seismic joint for San Francisco Bay Tunnel. J Struct Div 97(4):1129–1141

EAK (2000), Greek seismic code. O.A.S.P, Athens, 2001 (in Greek)

EC8 (2002) Eurocode 8: design of structures for earthquake resistance. European Committee for Standardization (CEN)

El Nahas A, Bransby MF, Davies MCR (2006) Centrifuge modelling of the interaction between normal fault rupture and rigid, strong raft foundations. In: Proceedings of international conference on physical modelling in geotechnics, Hong Kong, August, pp 337–342

Fukushima Y, Irikura K, Uetake T, Matsumoto H (2000) Characteristics of observed peak amplitude for strong ground motion from the 1995 Hyogoken Nanbu (Kobe) earthquake. Bull Seismol Soc Am 90:545–565

Gazetas G (1983) Analysis of machine foundation vibrations: state of the art. Soil Dyn Earthquake Eng 2(1):2–43

Gazetas G (1991) Foundation vibrations. In: Fang HY (ed) Foundation engineering handbook, Chap. 15, 2nd edn. Springer/kluwer, pp 553–593

Gazetas G (1996) Soil dynamics and earthquake engineering: case histories. Symeon Pub., Athens

Gazetas G, Anastasopoulos I, Dakoulas P (2005) Failure of harbor quaywall in the Lefkada 2003 earthquake. In: Proceedings of geotechnical earthquake engineering satellite conference—performance based design in earthquake geotechnical engineering: concepts and research, Osaka, pp 62–69

Gerolymos N, Gazetas G (2005) Constitutive model for 1-D cyclic soil behaviour applied to seismic analysis of layered deposits. Soils Found 45(3):147–159

Gilbert GK (1890) Lake Boneville. U.S. Geological Survey Monograph 1

Hashash YMA, Hook JJ, Schmidt B, Yao JI-C (2001) Seismic design and analysis of underground structures. Tunnel Undergr Space Technol 16(2):247–293

Horsfield WT (1977) An experimental approach to basement-controlled faulting. Geologie En Mijnboyw 56(4):363–370
Johansson J, Konagai K (2004) Fault induced permanent ground deformations—Simulations and experimental verification. In: Proceedings of the 13th world conference on earthquake engineering, August 1–6, Vancouver, Canada
Kelly JM (1997) Earthquake resistant design with rubber, 2nd edn. Springer
Kelson KI, Kang K-H, Page WD, Lee C-T, Cluff LS (2001) Representative styles of deformation along the chelungpu fault from the 1999 Chi-Chi (Taiwan) earthquake: geomorphic characteristics and responses of man-made structures. Bull Seismol Soc Am 91(5):930–952
Kiyomiya O (1995) Earthquake-resistant design features of immersed tunnels in Japan. Tunnel Undergr Space Technol 10(4):463–475
Kuesel TR (1969) Earthquake design criteria for subways. J Struct Div ASCE ST6:1213–1231
Lade PV, Cole DA, Jr., Cummings D (1984) Multiple failure surfaces over dip-slip faults. J Geotech Eng ASCE 110(5):616–627
Lazarte CA, Bray JD (1995) Observed surface breakage due to strike-slip faulting. In: Third international conference on recent advances in geotechnical engineering and soil dynamics, vol 2, pp 635–640
Luco JE, Wong HL (1986) Response of a rigid foundation to a spatially random ground motion. Earthquake Eng Struct Dyn 14:891–908
Marshall C (1999) The Øresund tunnel—making a success of design and build. Tunnel Undergr Space Technol 14(3):355–365
Okamoto S (1984) Introduction to earthquake engineering, 2nd edn, Tokyo University Press
O'Rourke MJ, Bloom MC, Dobry R (1982) Apparent propagation velocity of body waves. Earthquake Eng Struct Dyn 10:283–294
PB (1991) Trans-Bay tube seismic joints post-earthquake evaluation. Report prepared for the Bay Area Rapid Transit District, Parsons, Brinckerhoff, Quade and Douglas Inc
Potts DM, Dounias GT, Vaughan PR (1990) Finite element analysis of progressive failure of Carsington Embankment. Géotechnique 40(1):79–101
Potts DM, Kovacevic N, Vaughan PR (1997) Delayed collapse of cut slopes in stiff clay. Géotechnique 47(5):953–982
Poulos HG, Davis EH (1974) Elastic solutions for soil and rock mechanics. Wiley
Roth WH, Scott RF, Austin I (1981) Centrifuge modelling of fault propagation through alluvial soils. Geophys Res Lett 8(6):561–564
Sanford AR (1959) Analytical and experimental study of simple geologic structures. Bull Geol Soc Am 70: 19–52
Schnabel PB, Lysmer J, Seed BH (1972) SHAKE: a computer program for earthquake response analysis of horizontally layered sites. Report no. EERC 72/12, University of California, Berkeley, CA, USA
Slemmons DB (1957) Geological effects of the Dixie Valley-Fairview Peak, Nevada, Earthquakes of December 16, 1954. Bull Seismol Soc Am 47(4):353–375
St.John CM, Zahrah TF (1987) Aseismic design of underground structures. Tunnel Undergr Space Technol 2(2):165–197
Stein RS, Barrientos SE (1985) The Borah Peak Idaho earthquake-geodetic evidence for deep rupture on a planar fault. U.S. Geological Survey, Open-file report 85–250, pp 181–234
Taylor CL, Cline KMM, Page WD, Schwartz DP (1985) The Borah Peak, Idaho Earthquake of October 28, 1983—surface faulting and other phenomena. Earthquake Spectra 2(1):23–49
Trifunac MD, Todorovska MI, Lee VW (1998) The Rinaldi strong motion accelerogram of the Northridge, California, Earthquake of 17 January, 1994. Earthquake Spectra 14(1):225–239
Tselentis A (2004) Estimation of seismic hazard and seismic deformation of the Rion–Antirrion straits. Technical report to O.S.E., Earth Research Ltd, July 2004
Vrettos Ch (2005) Design issues for immersed tunnel foundations. In: Gazetas G, Goto Y, Tazoh T (eds) Proceedings of the 1st Greece-Japan workshop on seismic design, observation, and retrofit of foundations, pp 257–266
Witkind IJ, Myers WB, Hadley JB, Hamilton W, Fraser GD (1962) Geologic features of the earthquake at Hebgen Lake, Montana, August 17, 1959. Bull Seismol Soc Am 52(2):163–180